Testing and modelling of flow-drill screw connections under quasi-static loadings

Johan Kolstø Sønstabø[a,b], David Morin[a,b,*], Magnus Langseth[a,b]

[a]*Centre for Advanced Structural Analysis (CASA), Norwegian University of Science and Technology (NTNU), NO-7491 Trondheim, Norway*
[b]*Structural Impact Laboratory (SIMLab), Department of Structural Engineering, NTNU, NO-7491 Trondheim, Norway*

Abstract

The behaviour of a flow-drill screw connection under different quasi-static loadings was simulated using finite element models with detailed solid element meshes. The numerical models were developed with a rate-independent isotropic hypoelastic-plastic material model. A process-effect analysis was conducted, including investigation of the microstructure as well as hardness tests. Based on the investigation, the process effects were considered negligible. A simple approach for building up the geometry of the connection was presented. An experimental programme consisting of five different single-connector tests was carried out to characterise the connection, and was presented in detail. Each test was simulated, allowing for one-to-one comparisons between tests and simulations. Satisfactory results were achieved.

Keywords: Flow-drill screw, Connection, Finite element, Experiments, Automotive

1. Introduction

Flow-drill screws (FDS) are commonly used to join parts of dissimilar materials in the load-bearing structure of cars. Since connections play important roles for the crashworthiness of vehicles, knowledge about their physical behaviour under impact loadings is important for design decisions. Necessary knowledge and physical insight is usually gained through extensive experimental programmes, which typically involve loading specimens consisting of two or more plates joined with one or more connectors until failure (Sønstabø et al., 2015). Various loadings are achieved by changing the specimen design and loading directions.

A limited number of experimental studies on FDS connections can be found in the open literature. Szlosarek et al. (2013) presented a novel testing and analysis method. It was demonstrated for an FDS connection between plates of a carbon fibre reinforced polymer and aluminium. Skovron et al. (2014) studied the FDS process for a connection between sheets of aluminium alloy AA 5052-O. They explored feasible design space regions to determine how process parameters affect the geometry of the assembled connection. Mechanical tests were

*Corresponding author
Email address: david.morin@ntnu.no (David Morin)

performed to validate the findings. Sønstabø et al. (2015) carried out a large experimental programme to characterize an FDS connection between sheets of AA 6016 T4. The results were compared to equivalent tests on self-piercing rivet connections. Skovron et al. (2015) studied the effect of thermally assisting the FDS process (i.e. pre-heating the plates with an external heat source), and performed mechanical tests on a connection between sheets of AA 6063 T5A. Sønstabø et al. (2016) presented experiments on connections between an AA 6016 T4 sheet and an AA 6063 T6 extrusion, which they used to evaluate state-of-the-art macroscopic large-scale finite element modelling techniques. A *macroscopic model* here means a simplified model used to represent connections in large-scale analyses where time step restrictions prohibit detailed modelling of the connections. On the other hand, a *mesoscopic model* is a detailed three-dimensional finite element model with a fine solid mesh, where the actual geometry of the connection is taken into account.

To the best of the authors' knowledge limited scientific literature exist on mesoscopic modelling of FDS connections. A literature survey revealed one paper by Grujicic et al. (2016), who made an attempt to simulate the FDS process. The results from the process simulation were mapped to finite element models of different coupon tests. The global force-displacement curves from the coupon simulation results were qualitatively compared to corresponding curves from the experiments of Sønstabø and Holmstrøm (2013) which have been presented in the journal article of Sønstabø et al. (2015). These experiments were with a different screw and different plate materials.

In addition to complement experiments with additional information not otherwise achievable, a validated mesoscopic model of the connection may be used to explore the design space as function of e.g. thicknesses, materials and screw geometries in an efficient way, or for example to investigate particular deformation or failure modes. Another incentive for building a validated mesoscopic model is to use it for virtual testing of the connections. Experiments are costly and time consuming, and from an industrial perspective it would be beneficial to replace experiments with validated simulations. The results can for instance be used to calibrate macroscopic connection models for large-scale simulations.

Although little information is available for FDS connections, detailed numerical studies using mesoscopic models have been carried out on other connection types, some examples of which are presented in the following. Bouchard et al. (2008) used three-dimensional numerical models to study the behaviour of self-piercing rivet (SPR) connections under quasi-static loading conditions. They included mechanical properties obtained with two-dimensional axisymmetric riveting process simulations, and were in most cases able to reproduce the correct behaviour of the connection with reasonable accuracy in terms of force-displacement response and deformation mode. Chen et al. (2014) conducted a numerical and experimental study of a riveted joint, including the riveting process and tension tests, to investigate the failure modes under tensile loads. Kong et al. (2008) predicted the plastic and failure behaviour of a single lap-joint test of a resistance spot-weld between two steel sheets. Constitutive models were calibrated for different weld zones and coupled with a failure model. The finite element model was used to study the effect of nugget size and sheet thickness. A similar study was carried out by Nielsen

(2008), who used a modified Gurson material model to successively model plug failure for sufficiently large spot-weld diameter. Interface failure typically seen for smaller weld diameters was not well described. This was achieved later by Nielsen and Tvergaard (2010) by modifying an extension to the Gurson model. Sabuwala et al. (2005) used finite element analysis to study the behaviour of fully restrained steel connections subjected to blast loads. The results revealed that design criteria for steel connections subjected to blast loads were inadequate, and recommendations for modifications were presented. Liu et al. (2015) performed experimental tests to investigate the dynamic response of top-and-seat with web angle steel beam-column connections subjected to a sudden column removal. They employed three-dimensional finite element simulations to understand the deformation and failure mechanisms that were observed in the experimental tests.

Numerical simulations of the FDS process are difficult to set up. The process physics are complex, involving for instance friction, large plastic deformations and thermal softening. A coupled thermo-mechanical finite element model would be required, and accurate description of the different phenomena would be difficult. Moreover, the large deformations would cause numerical challenges, introducing the need for e.g. remeshing. In addition, one would need data of the process input parameters, e.g. rotational speed, torque and driving force. Besides, such a process simulation would be difficult to validate.

The present article explores the possibilities of modelling FDS connections between aluminium plates with a mesoscopic model, without taking the process into account. The developed numerical model was validated using experiments, both with respect to deformation modes and force-deformation characteristics. A simple approach for building up a sufficiently accurate model is presented. Five different finite element models were built up, each one resembling an experimental test, allowing for direct comparisons between simulations and experiments. The experimental programme consisted of cross tension, cross mixed, cross shear, single lap-joint and peeling tests. The novelty of this paper is related to the mesoscopic modelling of FDS connections, as well as the validation carried out using a new cross test set-up.

The experiments are explained and presented first, followed by a discussion about process effects. The finite element model is subsequently presented, and finally the simulation results are discussed.

2. Experiments

The term *connection* is in the present article defined as *a system that mechanically fastens two or more parts together* (Sønstabø et al., 2015, 2016), implying that it consists of the screw itself plus some surrounding plate materials. The connection investigated in this work consisted of an M5 through-hardened steel screw connecting a 2 mm thick rolled sheet of AA 6016 in temper T4 to a 2 mm thick extrusion of AA 6063 in temper T6. A schematic drawing with nominal dimensions and a cross-section picture of the connection are presented in Fig. 1. This material combination was chosen since it is representative of a typical FDS connection in cars, with the top sheet having a yield stress of approximately 120 MPa and the bottom extrusion a yield stress of approximately

210 MPa. A pre-hole of 7 mm diameter was used in the top plate. Engineering stress-strain curves for the plate and screw materials are presented in Fig. 2. As seen, the extrusion (6063) had a higher yield stress, but the rolled sheet (6016) had stronger work-hardening and was significantly more ductile.

The connection was studied by means of cross tests in three loading directions (tension, shear, and combined tension and shear), and single lap-joint and peeling tests. Schematic drawings of the test specimens are presented in Fig. 3, where clamped areas are indicated with grey colour. The dark grey colour in Fig. 3a indicates where a smaller clamp was used in the cross mixed and shear tests. All tests were quasi-static. Three to five repetitions were carried out for each test. The global responses (force-displacement curves) are reported, together with detailed descriptions of the tests and post-mortem pictures of specimens. The global response in the single lap-joint and peeling tests has been briefly reported before (Sønstabø et al., 2016).

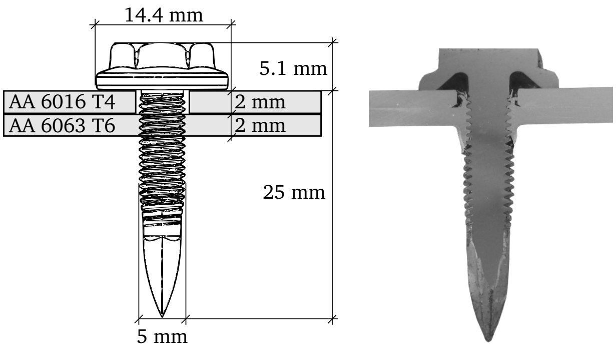

(a) (b)

Fig. 1. FDS connection. (a) Schematic drawing. (b) Picture of the cross-section.

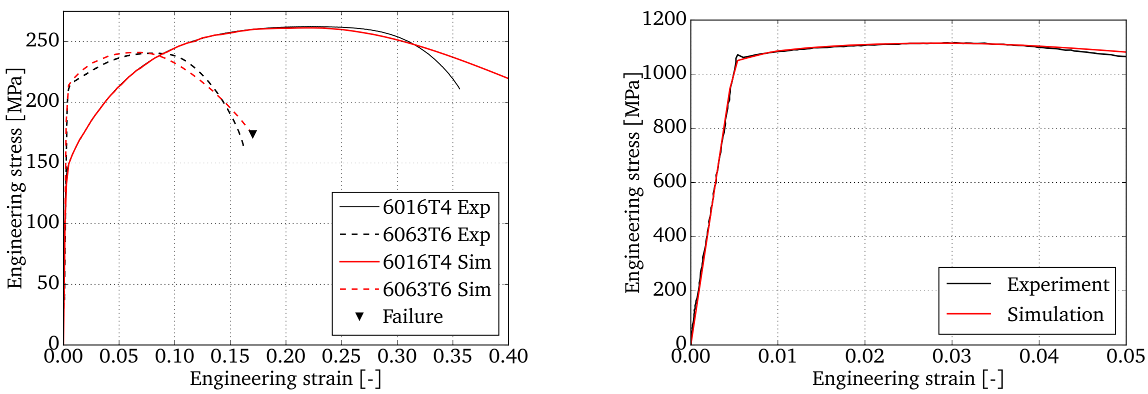

(a) (b)

Fig. 2. Engineering stress-strain curves for the (a) plate materials and (b) screw material. Curves from simulations of the material tests are included (see Section 4.2).

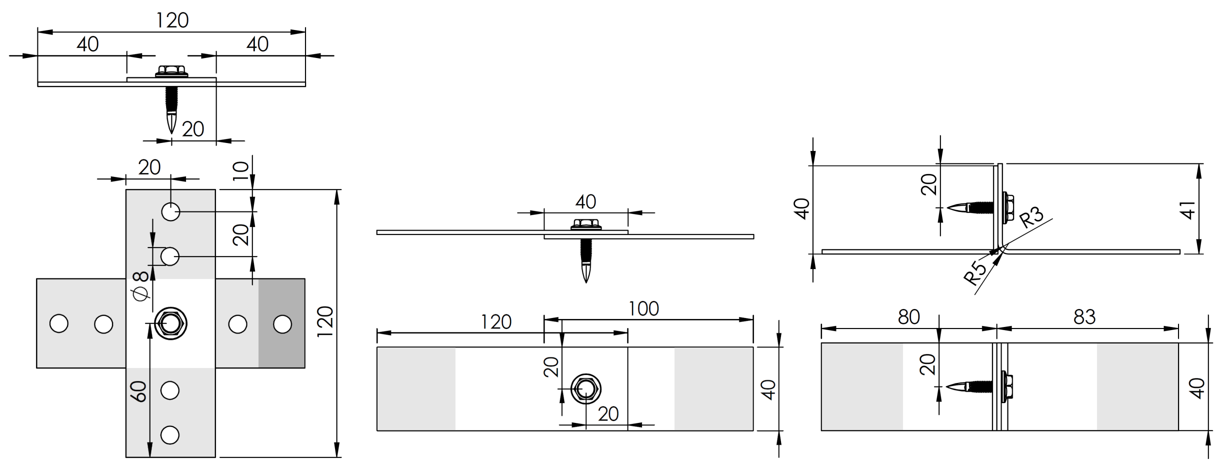

(a) (b) (c)

Fig. 3. Drawings of test specimens. (a) Cross test. (b) Single lap-joint test. (c) Peeling test. Clamped areas are coloured grey. The dark grey colour in (a) indicates the area where a smaller clamp was used in the cross mixed and cross shear tests.

2.1. Cross tests

Fig. 4a illustrates the principle of the cross tests. The coloured areas in the figure were clamped in the tests. The red parts were fixed, while the blue parts were pulled in the directions of the arrows corresponding to tension-, mixed- and shear loading. To allow for relative sliding of the plates, only half of the area on one side of the bottom plate was clamped in the cross mixed and shear tests. This is indicated with a lighter red colour where the clamping was omitted. The bottom plate was fixed, while the top plate was pulled in the direction of the arrows in the figure.

Fig. 4b shows a principle drawing of the cross tension test set-up. The specimen was mounted on two steel fixtures, using screws and clamping blocks. A picture of the set-up is shown in Fig. 4c. The steel fixtures were placed in a regular Instron tensile testing machine, where they were pulled apart in the vertical direction. Pure tensile loading was ensured by hinging the fixture in each end. The pulling force was measured with a load cell mounted in series between the top fixture and the cross beam of the testing machine. A camera was used to take photographs during the tests to record the relative displacement of the steel fixtures with a digital image correlation (DIC) method (readers are referred to Fagerholt (2012) for details on DIC). Black and white checkerboard markers were glued on the steel fixtures, for the DIC analysis.

The shear and mixed mode cross tests were carried out using the rig shown in Figs. 4d to 4f. The test rig was designed so that it was easy to control the support conditions, such that a one-to-one relationship with numerical boundary conditions could be obtained. Principle drawings of the set-up are shown in Figs. 4d and 4e, and Fig. 4f shows a picture of the mixed-mode set-up. The cross specimen was clamped to two main steel parts (denoted as part 1 and part 2 in Fig. 4) with screws and clamping blocks. The main steel parts were placed inside a cylindrical steel casing, to control their motion, thus ensuring controlled boundary conditions in the test. Part 1

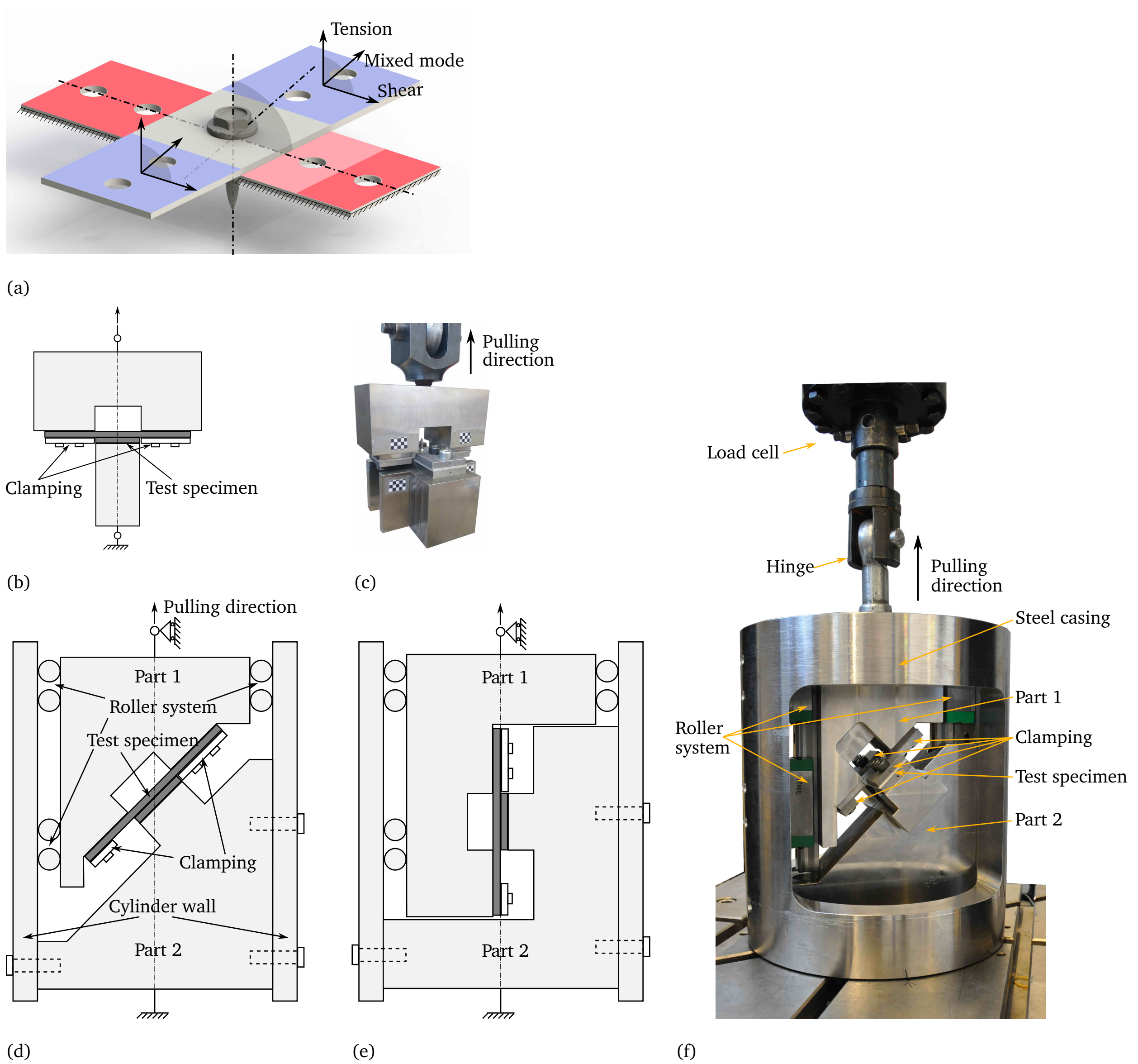

Fig. 4. Illustrations of the set-ups in the cross tests. (a) Principle of the cross tests. (b) Principle drawing of the tension set-up. (c) Picture of the tension set-up. (d) Principle drawing of the mixed-mode set-up. (e) Principle drawing of the shear set-up. (f) Picture of the mixed mode set-up.

was attached to the cylinder with a roller system, allowing for smooth motion in the loading direction, whereas part 2 was bolted to the casing.

The rig was placed in a regular Instron tensile testing machine. The rig was hinged in the top, and attached to the testing machine with a single bolt between the centre of the bottom of part 2 and the testing machine. A load cell was mounted between the top hinge and the cross-beam of the testing machine. It was confirmed by in-house testing that the friction forces in the rollers were negligible compared to the pulling force, and thus that the force measured was equal to the force transmitted through the specimen. The clamping was carefully monitored to verify that no slipping occurred. A camera was used to take photographs during the tests. The pictures were used to monitor the rigid-body motion of parts 1 and 2 using DIC. Black and white checkerboard markers were glued on parts 1 and 2, for the DIC analysis. It was verified that the rotation and translation in other directions than the pulling direction were negligible. The cross-head velocity in all cross tests was set to 5 mm/min, which was assumed to render quasi-static conditions.

All three cross test set-ups were designed such that the load application line passed exactly through the centre of the specimen (as indicated with stippled-dotted lines in Figs. 4a, 4b, 4d and 4e).

Force-displacement curves from the cross tests are shown in Fig. 5 and deformed specimens are depicted in Figs. 6a to 6d. The displacement plotted here is the relative displacement between parts 1 and 2 which was measured with DIC. As seen, the connection was strongest in shear and weakest in tension. The shear mode exhibited highest ductility while the tensile mode exhibited lowest. The mixed mode response showed intermediate force level and ductility. Large variation in initial stiffness was seen for the mixed mode and shear tests. This was due to the pre-hole which allowed for relative sliding between the top and bottom plate under shear loading. The force required to give sliding varied from specimen to specimen, which might be due to variations in the screw-driving process (e.g. pre-stressing, surface finish, cleanliness). Apart from this variation the repeatability of the test results was acceptable.

In tension significant plate yielding caused a distinct knee in the force-displacement curve after approximately 1 mm displacement. The force increased until approximately 3.2 kN where the threads were stripped from the

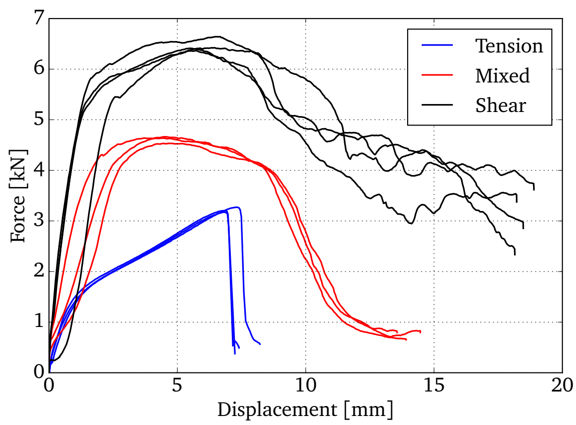

Fig. 5. Force-displacement curves from cross tests.

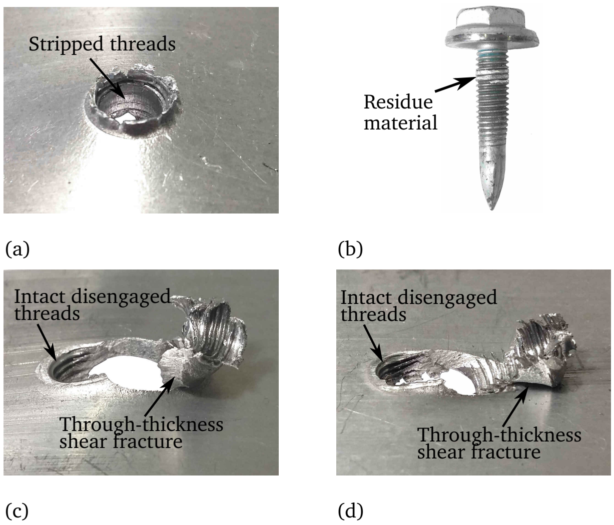

Fig. 6. Photographs of representative post mortem specimens from cross tests. (a) Cross tension, top side of bottom plate. (b) Cross tension, screw. (c) Cross mixed mode, top side of bottom plate. (d) Cross shear, top side of bottom plate.

bottom plate. This is clearly seen in Figs. 6a and 6b, where residue material from the stripped threads is seen on the screw. There were limited deformation of the top plates, therefore they are left out from Fig. 6.

A stiffer response was observed for the mixed mode tests. The force reached a maximum of approximately 4.6 kN. Fig. 6c indicates that the main failure mechanism was through-thickness shear fracture of the bottom plate material. The tangential component of the displacement of the top plate pushed the screw sideways such that the threads were engaged only on one side of the hole. Fig. 6c clearly shows intact disengaged threads on the left side of the hole and through-thickness shear fracture on the right.

The connection gave stiffest response under pure shear loading. The maximum force was approximately 6.5 kN. As for the mixed mode tests the tangential displacement pushed the screw sideways and disengaged the threads on one side. Fig. 6d indicates that failure occurred by through-thickness shear fracture of the bottom plate. Slight plastic bending of the screw shaft was observed for some of the cross shear tests.

There was no clear end of the pure shear tests. In pure tension and mixed mode, the end of test was clearly seen as the force dropped to nearly zero and the plates were completely separated. This was not the case under pure shear loading (see Fig. 5). As the cross shear specimen was deformed the screw rotated and tried to push the plates apart. However, the steel casing of the testing rig prevented any motion other than the pulling direction, with the consequence that the screw was squeezed between the plates. Thus the force level did not drop to zero even after fracture took place, probably due to high frictional and contact forces between the screw and plates.

The top plate did not experience failure in any of the tests, only plastic deformations. They are therefore not depicted.

2.2. *Single lap-joint and peeling tests*

The single lap-joint and peeling tests were done using the set-up described by Sønstabø et al. (2015), who carried out similar tests for a different connection. The specimens (illustrated in Figs. 3b and 3c) were clamped in a standard Instron tensile test machine using mechanical grips with a clamping length of 40 mm. The clamps were centred along the load application line, such that the single lap-joint specimen was slightly deformed during clamping (this is illustrated in Fig. 7). The deformation was purely elastic. The force was measured using an Instron load cell and the displacement was recorded from the cross-head displacement of the test machine. The cross-head velocity was set to 10 mm/min.

The force-displacement response in the single lap-joint tests (Fig. 8a) was similar to the cross shear test. The maximum force was slightly lower (approximately 5.9 kN) and the ductility was comparable. A clear failure

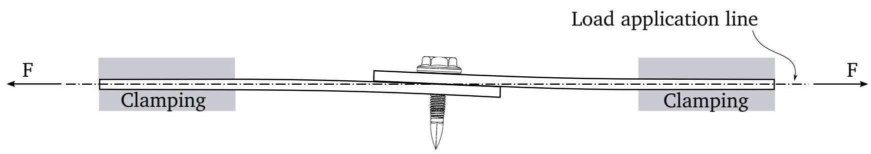

Fig. 7. Illustration of clamping in the single lap-joint test.

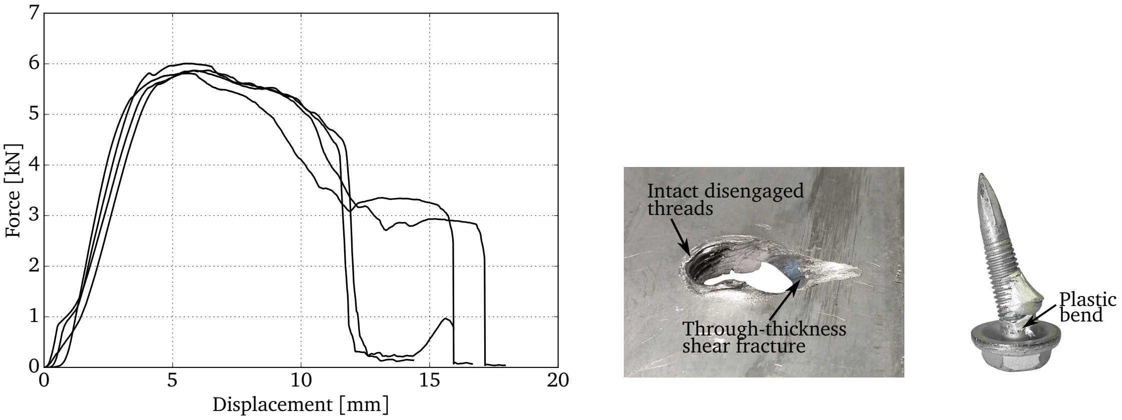

(a) (b) (c)

Fig. 8. Results from single lap-joint tests as (a) force-displacement curves, and representative post-mortem pictures of (b) top side of bottom plate and (c) screw.

was seen in the force curves, probably due to less restrictive clamping than in the cross shear tests. The simpler clamping conditions allowed the plates to bend more, possibly rotating the entire connection. This probably introduced tensile loading on the connection. Significant scatter is seen for the displacement at failure, which is not uncommon for tests on connections such as FDS. As for the cross mixed and shear tests the presence of the pre-hole caused large variation in initial stiffness. Parts of post-mortem specimens are depicted in Figs. 8b and 8c. As seen, the failure mechanism was similar to the cross shear tests, with through-thickness shear fracture of the bottom plate. Significant plastic bending of the screw shaft occurred in the single lap-joint tests.

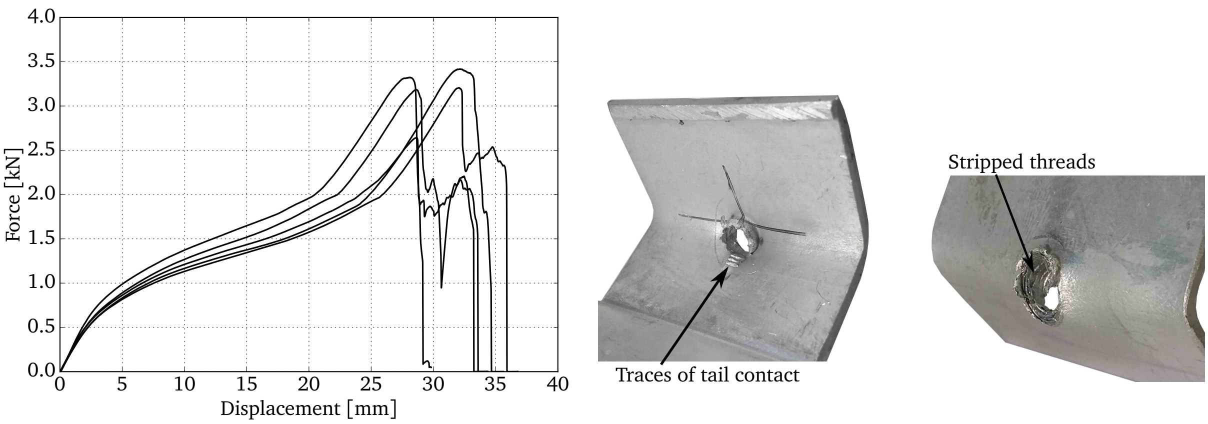

(a) (b) (c)

Fig. 9. Results from peeling tests as (a) force-displacement curves, and representative post-mortem pictures of (b) top side of bottom plate and (c) underside of bottom plate.

Fig. 9a shows the force-displacement curve from the peeling tests. A knee was observed after ca. 2.5 mm displacement, caused by yielding of the plate materials. The force gradually increased up to 2 kN where the slope abruptly increased due to contact between the shaft of the screw and the bottom plate (traces of the contact is visible in Fig. 9b). Some variation was evident in the force level as well as in the displacement at the time of shaft contact. These variations were probably caused by discrepancies in the position of the screw. The maximum force was approximately 3.2 kN and failure occurred by thread stripping in the bottom plate (see Fig. 9c).

3. Process effects

In the FDS process flow-drilling and thread forming is combined into a single procedure where the screw is both used as tool to generate the hole and as fastener. The process (illustrated in Fig. 10) consists of the following six stages (Skovron et al., 2014; Sønstabø et al., 2015): *heating*, *penetration*, *extrusion forming*, *thread forming*, *screw driving* and *tightening*. In the heating stage the screw is forced against the plate material while rotating (usually 2000-6000 rpm) to heat up the material. Subsequently an increasing downward force is applied and the screw penetrates the plate. Material flows up and down along the length of the screw and forms a boss (material that flows upwards between the plate and the screw head). When the tail of the screw pierces the bottom surface of the plate a so-called extrusion is formed as material flows downwards along the screw shaft. Threads are created by a thread-forming zone on the fastener, and the screw is driven in until the head hits the top plate. A final torque is applied to a pre-set value in order to ensure a tight connection. The whole process usually takes between 1.5 and 4 seconds, depending on the material combination, plate thickness and type of screw.

During the process the plate material close to the screw simultaneously undergoes a temperature increase and significant plastic straining. The plastic straining leads to a work-hardened zone of unknown size. Skovron

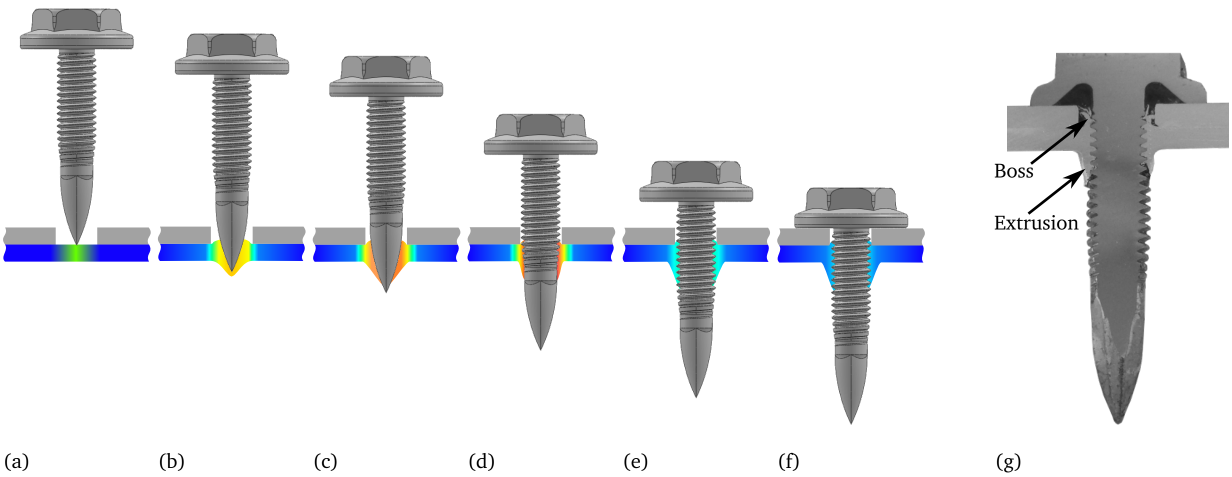

Fig. 10. The FDS process. (a) Heating. (b) Penetration. (c) Extrusion forming. (d) Thread forming. (e) Screw driving. (f) Tightening. A picture of an FDS connection is shown in (g), with the boss and extrusion indicated.

et al. (2014) measured the surface temperature during the process for different fastener forces (which is inversely related to the temperature), and reported temperatures between 150 °C and 330 °C. The increased temperature may have two consequences. First, it leads to thermal softening which reduces the resistance against the plastic deformations during the process, which would facilitate penetration of the screw into the bottom plate. Second, the higher temperature might lead to permanent changes in mechanical properties of the aluminium alloy. This would imply that there is a process-affected zone of unknown size due to the process.

As explained in Section 4, potential process effects were neglected in the simulations. To assess this assumption, a study consisting of a microstructural analysis and Vickers hardness tests was carried out and is presented in the following.

3.1. Microstructural Analysis

Fig. 11 presents a metallographic photograph of the bottom plate cross-section (excluding the screw), where different colours indicate particular grain orientations. Various details are highlighted by zoomed-in pictures. When examining the pictures it is seen that the grains are markedly deformed close to the screw, implying that large plastic strains have occurred during the process. The deformation appears to be most severe near the surface of the threads (closest to the screw). Inside the boss and extrusion all grains seem deformed. This was expected, since these areas were formed by plastic material flow during the process. In the internal area close to the screw the deformations seem less severe, except for very close to the screw. At a distance of approximately 0.5 mm (one thread-width) away from the screw the grains are seemingly undeformed (see lower left part of Fig. 11). This observation indicates that the plastic deformations are localised and that the width of the plastically deformed zone is small.

3.2. Vickers Hardness Tests

Vickers hardness tests were carried out on the cross-section surface of the bottom plate to further study the effect of the process. The measurements were done with HV0.5 with 0.5 mm distance between dents. This produced dents with a diameter of approximately 115 µm. A smaller weight and denser indenting pattern (micro hardness) were not desirable as individual grains would be indented. The results would then be more affected by the different grain orientations and produce more scatter. The grain size for this alloy typically ranges from 60 to 80 µm (Fig. 11). The measurements were done along two horizontal and one vertical line on both sides of the screw. Fig. 12a shows the measurement locations and illustrates the naming convention used to identify the individual dents. Each row was assigned a label (e.g. A2), and a location number. As an example, point A2-14 corresponds to the leftmost dent in the upper horizontal line on the left side.

The results show no significant variation in hardness in the horizontal direction away from the screw (Fig. 12b), except points A1-1 and B1-1 where a somewhat lower hardness was measured. These points were closest to the screw, located in the area between two threads. The measurements in the vertical direction along

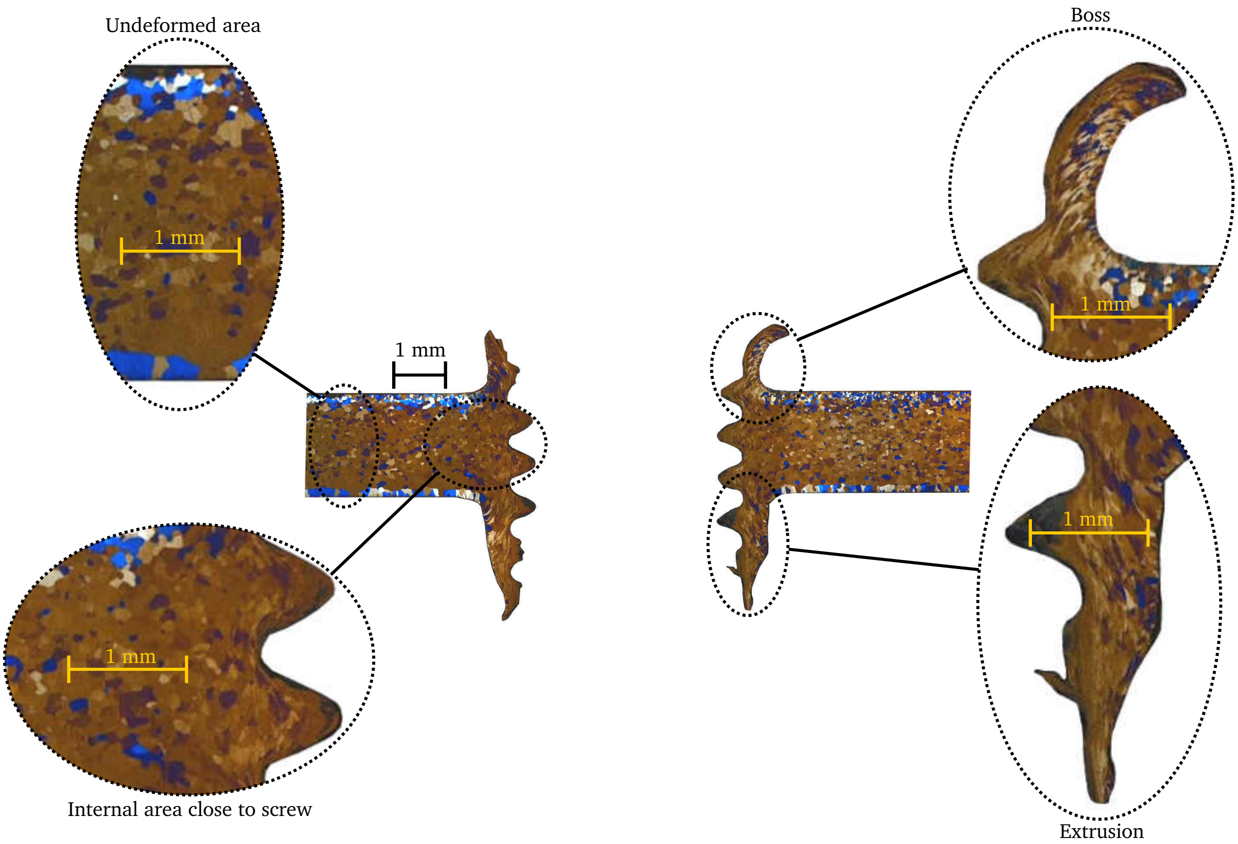

Fig. 11. Metallographic photograph of a cut FDS cross-section excluding the screw. Zoomed-in details are included.

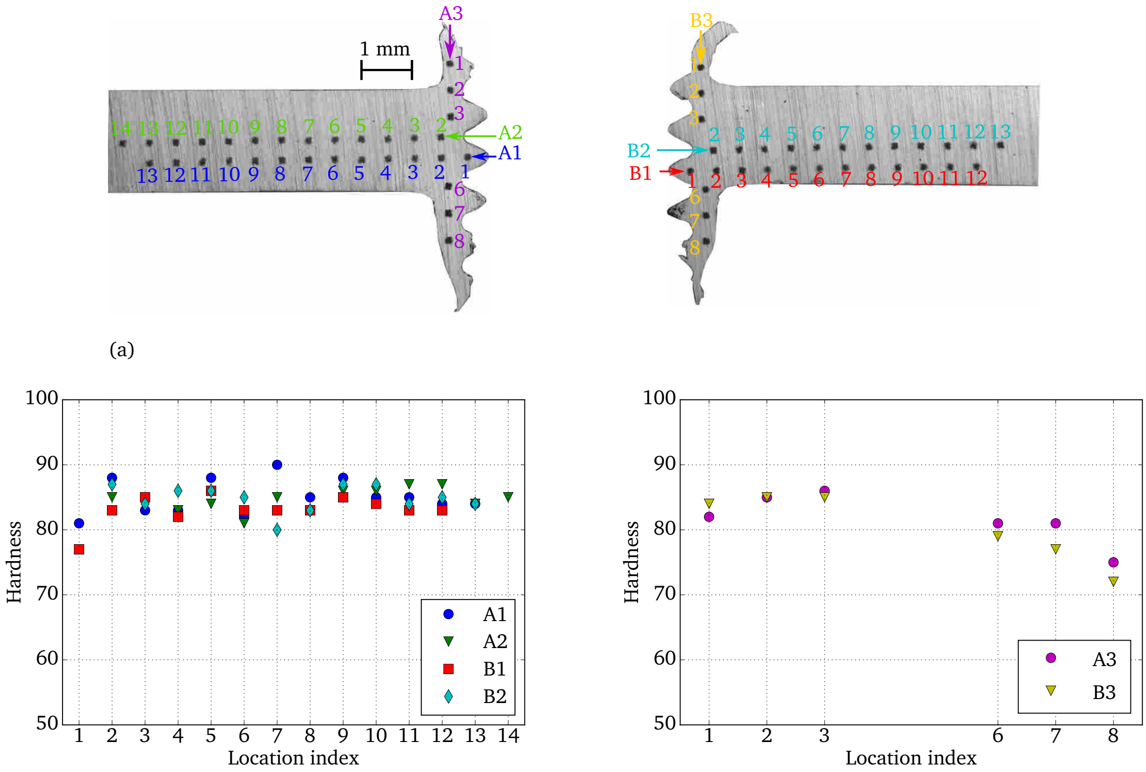

(a)

(b)

(c)

Fig. 12. Vickers hardness tests. (a) Dent locations. (b) Hardness values along horizontal lines. (c) Hardness values along vertical lines.

the boss and extrusion are given in Fig. 12c. Insignificant variation was observed for the three uppermost points (location 1, 2 and 3), compared to measurements far away from the screw in Fig. 12b, while somewhat lower hardness was measured for the three lowermost points (location 6, 7 and 8). It is noted that points A1-1, B1-1, A3-1, A3-8, B3-1 and B3-8 were close to the free edge which might affect the measured hardness for these points. The results from the Vickers hardness tests conform to findings by Skovron et al. (2014) and support the hypothesis that the process-affected zone is small.

4. Numerical model set-up

4.1. Finite element models

In this section the finite element models and the material models used are presented and discussed.

A circular finely meshed model of the connection was generated and tied to five more coarsely meshed models corresponding to the five experimental tests (see Fig. 13). The connection model was generated as follows. Three parts were defined: the screw, the bottom plate and the top plate. Because the precise geometry of the screw was unknown an approximate geometry was measured using a simple camera technique, illustrated in Fig. 14. A screw was cut in half and a computer programme used to measure the outline of the screw cross-section from a picture, which was subsequently utilised to revolve a 3D part. This operation implies that the helix shape of the threads was neglected. This simplification was studied by Chen and Shih (1999), who observed small changes in the load distribution compared with including the helix shape, but otherwise similar results. The outer edge of the boss and extrusion of the hole in the bottom plate was modelled in a general way by straight lines and circular arcs (see magenta lines in Fig. 15), and their dimensions were chosen based on the picture in Fig. 1b. The bottom plate was generated without a hole, and the screw was positioned in place such that the two parts overlapped. The overlapping volume was then removed from the bottom plate, such that a hole with identical geometry as the screw was generated, including internal threads. With this technique the internal threads of the bottom plate coincided with the external threads of the screw, which facilitates the meshing operation. Hence possible gaps between the screw and bottom plate were not accounted for. The top plate was modelled with a pre-hole of 7 mm diameter.

The screw was discretised using 10-node modified quadratic tet elements, while the plates were comprised of 8-node hex elements with reduced integration. As seen in Fig. 15, a fine mesh was required to resolve the geometry of the threads. The smallest element size of the bottom plate was approximately 0.03 mm, while the coarse parts were modelled with five elements through the plate thickness.

Fig. 16 illustrates the finite element models corresponding to the five tests. Figs. 16a and 16b show which parts of the cross specimens that were modelled. As seen, only the deformed part of the specimens were included (clamped areas were omitted), and displacements were prescribed on the surfaces corresponding to the clamped parts. For the bottom plate prescribed displacements were zero (fixed surfaces), while for the top plate they were zero in all directions except in the loading direction where a displacement was applied (indicated with arrows in Figs. 16c to 16g). The deformation during clamping in the single lap-joint tests was accounted for by applying a

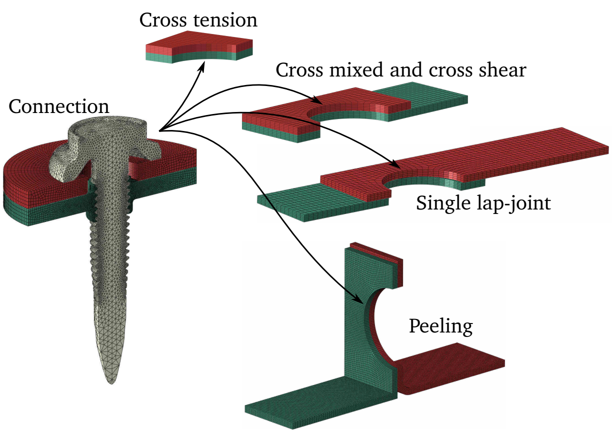

Fig. 13. Illustration of how the connection mesh was inserted into coarser specimens with tie constraints.

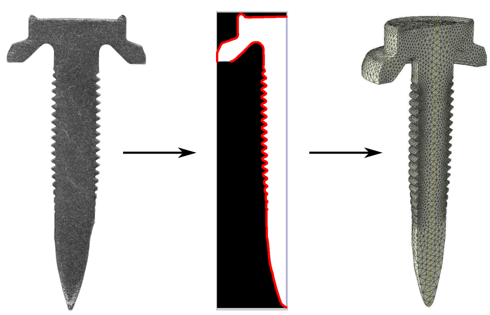

Fig. 14. Illustration of how the geometry of the screw part was generated.

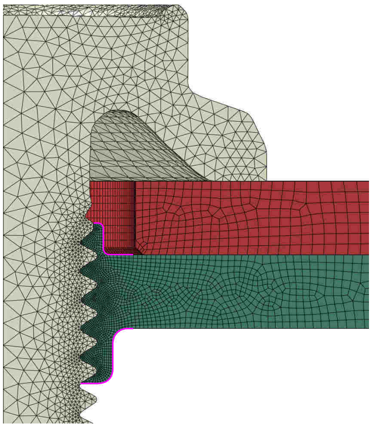

Fig. 15. Half cross-section of the finite element model.

2 mm displacement perpendicular to the loading direction before the main loading was applied (see Fig. 7).

The simulations were carried out using the Abaqus v6.11 explicit solver with double precision. Symmetry was utilised where possible, mass scaling was applied (inertia effects were ensured negligible), and a general surface-to-surface contact algorithm was used between the different parts. A friction coefficient of 0.1 was chosen. For reference, Porcaro et al. (2006) chose a friction coefficient of 0.15. Prescribed displacements were applied with a smooth amplitude. Fracture was modelled with element erosion.

4.2. Material model

The aluminium plates and steel screw materials were modelled using a rate-independent isotropic hypoelastic-plastic material model. It is, however, well known that the herein used aluminium alloys exhibit orthotropic plastic anisotropy, for instance as shown by Lademo et al. (1999), Lademo et al. (2009) and Sønstabø et al. (2016). To obtain a more accurate description of local deformations one could use anisotropic phenomenological plasticity or even crystal plasticity together with the finite element method. The crystallographic texture varied through the thickness of the 6063-extrusion (Fig. 11). Khadyko et al. (2016) showed that a very similar 6063-extrusion had a central layer with approximately cube orientation, an intermediate layer with random texture, and a small outer layer with Goss orientation. In spite of this an isotropic phenomenological plasticity material model was chosen in this work. A more advanced anisotropic phenomenological yield function or a crystal plasticity material model would greatly increase the computational time, due to the large number of elements in the mesh. It would require three different yield surfaces through the thickness. In addition, the mesh size was some places smaller than and some places larger than the grain size. Moreover, the global results of the simulations in this work were satisfactory, which indicates that the anisotropy of the material does not affect the global behaviour in a significant way. Therefore the marginal improvements crystal plasticity or a more advanced phenomenological yield surface could bring, do not justify the increase in computational time.

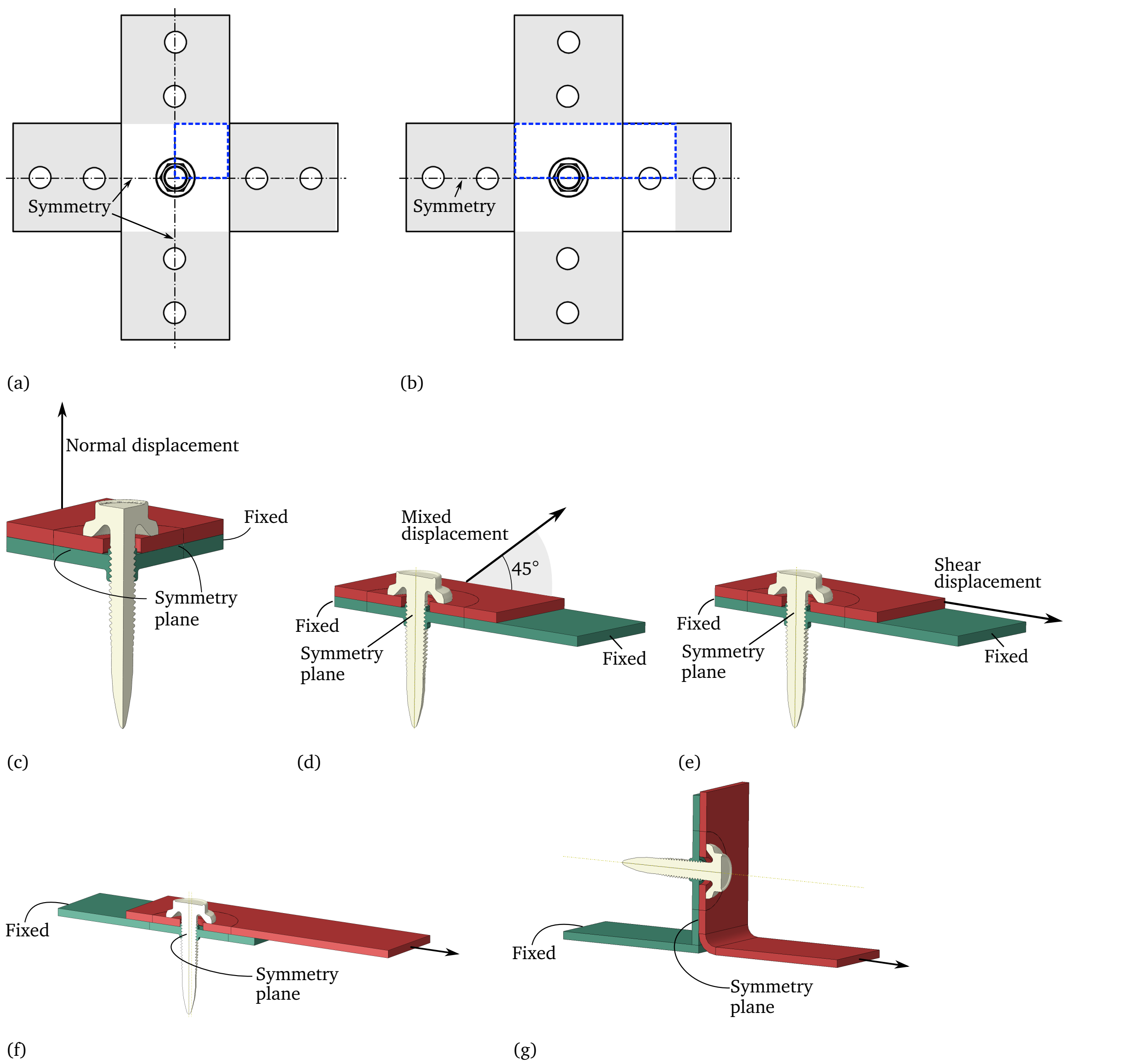

Fig. 16. Illustration of how each test was modelled. (a) and (b) shows which parts of the cross specimens that were modelled. (c) Cross tension model. (d) Cross mixed model. (e) Cross shear model. (f) Single lap-joint model. (g) Peeling model.

To model plasticity the von Mises yield surface was used, associated flow assumed, and isotropic hardening applied. The yield function may be written as

$$f = \sigma_{\mathrm{eq}} - (\sigma_0 + R) \leq 0,$$

where σ_{eq} is the von Mises equivalent stress, σ_0 is the initial yield stress, and R is an isotropic hardening variable. The Voce hardening law was selected,

$$R = \sum_{i=1}^{N} Q_{\mathrm{R}i}\left(1 - \exp\left(-\frac{\theta_{\mathrm{R}i}}{Q_{\mathrm{R}i}} p\right)\right), \tag{1}$$

where p is the equivalent plastic strain, N is the number of terms used, and $Q_{\mathrm{R}i}$ and $\theta_{\mathrm{R}i}$ are the saturation stress and initial hardening modulus for term i, respectively. Two terms were sufficient for the bottom plate while three terms were needed for the top plate and screw material.

In the experiments material fracture took place only in the bottom plate, the top plate and screw material did not fail. To model fracture in the bottom plate, element erosion with the Cockcroft-Latham criterion (Cockcroft and Latham, 1968) was included for this part. The criterion states that failure occurs when the integral

$$W = \int_0^p \langle \sigma_1 \rangle \, \mathrm{d}p \tag{2}$$

attains a critical value W_{C}. Here σ_1 is the maximum principal stress and $\langle \cdot \rangle$ denotes the Macauley brackets. Hence damage grows for a positive principal stress only. The criterion is easy to calibrate from a single uniaxial tensile test and was chosen for its simplicity.

The procedure to calibrate the initial yield stress and hardening parameters for the plate materials has been reported by Sønstabø et al. (2016). The parameters were obtained by reverse engineering uniaxial tensile tests with finite element simulations. Fig. 2a shows adequate correlation between tests and simulations.

The critical failure value W_{C} was obtained from the uniaxial tensile test simulation of the bottom plate material, by calculating the integral in Eq. (2) in the most critical element when the nominal strain in the simulation matched the experimental nominal strain at time of fracture (see Fig. 2a). The mesh size in the neck area of the tensile simulation was approximately 0.06 mm. It is known that W_{C} is a mesh size dependent parameter, due to increased strain gradients for denser meshes (Björklund et al., 2013). The mesh size dependency was, however, not accounted for here, one value for W_{C} was used for all elements, which was considered representative for the mesh size where fracture took place in the FDS simulations. Fig. 17 shows the resulting failure loci for generalised tension ($L = -1$), generalised shear ($L = 0$) and generalised compression ($L = 1$), where L is the Lode parameter defined as $L = -\cos 3\theta_L$ and θ_L is the Lode angle.

The screws were subjected to limited plastic deformations, and a simpler approach could be used to calibrate the hardening parameters. Uniaxial tensile tests of the screw material were carried out, using axisymmetric specimens which were cut out from the screw shaft (resulting engineering stress-strain curve is shown in Fig. 2b).

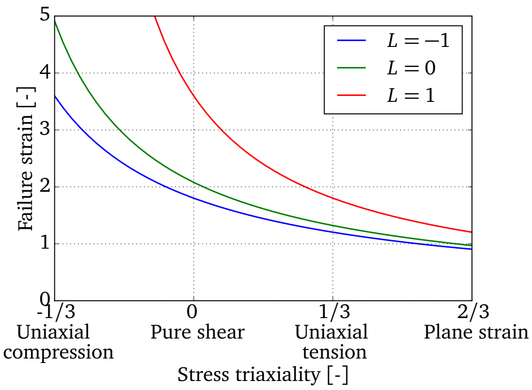

Fig. 17. Cockcroft-Latham failure loci for generalised tension ($L = -1$), generalised shear ($L = 0$) and generalised compression ($L = 1$).

The nominal strain was measured using an extensometer, and a digital camera was employed to track the diameter of the specimen. The post-necking plastic strain was calculated from the diameter measurements assuming plastic incompressibility. The post-necking equivalent stress was approximated using Bridgman correction (Bridgman, 1944), where the radius of the neck was measured from the digital images. Eq. (1) was then fitted to the obtained equivalent stress-plastic strain curve. Fig. 2b shows the result from a simulation of the material test using the obtained hardening parameters. As seen, the correlation was excellent for the relevant strain level.

Typical steel and aluminium values were used for the Young's modulus E and the Poisson ration ν. The material model parameters are summarised in Table 1.

4.3. *Process effects*

Possible process effects were discussed in Section 3. Metallographic photographs and Vickers hardness tests indicated that there was a local process-affected zone extending approximately 0.5 mm from the screw into the bottom plate. In the present finite element models, process effects were not taken into account. Satisfactory results were nevertheless obtained, which indicates that the process effects do not significantly affect the global behaviour.

Table 1

Material model parameters for the screw and plate materials.

	E [MPa]	ν [-]	σ_0 [MPa]	Q_{R1} [MPa]	θ_{R1} [MPa]	Q_{R2} [MPa]	θ_{R2} [MPa]	Q_{R3} [MPa]	θ_{R3} [MPa]	W_C [MPa]
Screw (steel)	210000	0.3	1051.1	16.8	12507	89.6	5726	1885	267	-
Top plate (AA 6016 T4)	70000	0.35	117.6	29.2	25000	149.5	2011	100	230	320
Bottom plate (AA 6063 T6)	70000	0.35	204.6	8.0	12300	55	1472	-	-	-

5. Simulation results

In this section the results from the finite element simulations of the experimental tests are presented and discussed. Global force-displacement curves are graphed, the simulated deformation modes and failure mechanisms are explained, and various field variables are plotted when needed for discussion. The cross test simulations are presented first, followed by the single lap-joint and peeling test simulations.

Overall good agreement was obtained between the simulations and experiments, both in terms of force-displacement responses and deformation modes, despite the simplifications made in the model (see Section 4).

5.1. Cross test simulations

As discussed in Section 2.1, variations in initial stiffness in the cross mixed and cross shear experiments occurred due to the pre-hole in the top plate, which allowed for relative sliding between the top and bottom plates (recall Fig. 5). The force required for sliding to occur was different from specimen to specimen, and was a function of unknown process parameters and the amount of prestress in the screw. Therefore this sliding could not be captured accurately by the finite element models. Acknowledging that the simulations did not capture the sliding accurately, it was chosen to shift the cross mixed and shear experimental curves to match the displacement of the simulations at 2 kN force. By doing this, the effect of the relative sliding in the experiments, and the poor representation of it in the simulations, was eliminated. It was assumed that all sliding occurred before 2 kN force was reached, and thus that the results afterwards could be compared. The shifting is illustrated in Fig. 18, which shows the start of the curves without and with shifting of the experimental curves. As seen, all shifted curves coincide at 2 kN force.

The force-displacement response from the cross test simulations are compared to the experimental results in Fig. 19, with the mixed and shear experimental curves shifted as explained above. As shown, overall satisfactory results were obtained. The force levels and shape of the curves match well with the experiments.

Throughout the cross tension test simulation the initial stiffness and force level were somewhat higher than in the experiments. Good agreement was obtained for the displacement at global failure. The overall deformation mode and failure mechanism of the specimen agreed with the experiment. As the bottom plate was bent upward the topmost threads were disengaged such that the three bottommost carried all the load. This is seen in Figs. 20a and 20b where the equivalent plastic strain field is plotted on the initial and deformed configurations a short instance before failure, which occurred by fracture in the threads. Agreement in deformation and failure mode with the experiment may be seen when comparing Fig. 20b with Fig. 6a.

The over-estimated stiffness in the cross tension simulation may indicate inaccuracies in the boundary conditions. In the experiment the plates were subjected to membrane forces and bending, which could lead to some deformation of the material in the edge of the clamping, which was not accounted for in the finite element model. In an effort to evaluate this effect, a finite element model with a simple model of the clamping was

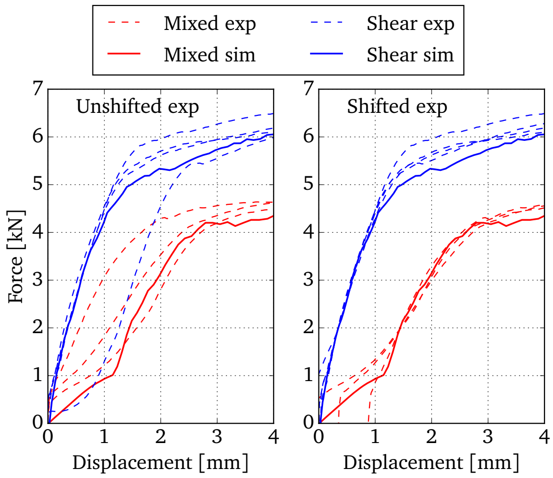

Fig. 18. Illustration of shifting of cross mixed and cross shear experimental curves.

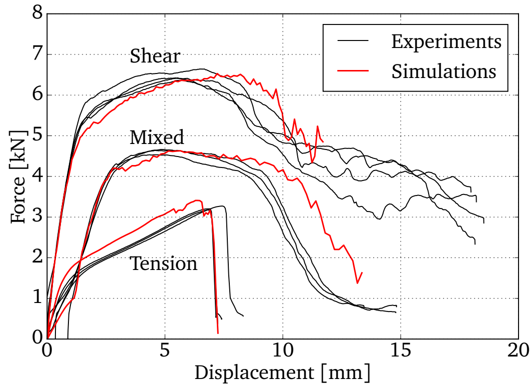

Fig. 19. Force-displacement curves from cross test simulations compared to experiments.

made, see Fig. 21a. The clamps were modelled as rigid, and the clamping was handled by increasing the friction coefficient to 0.6 between the clamps and plates, which ensured little slipping. The result is graphed in Fig. 21b and shows better agreement for the initial stiffness and force level, suggesting that the overestimated stiffness and force by the constrained model was indeed caused by inaccurate boundary conditions. The maximum force was, as expected, unchanged.

In cross shear and mixed mode excellent agreement in stiffness and maximum force level was achieved when accounting for the pre-hole sliding. Deformed specimens with equivalent plastic strain fields on initial and deformed configurations are shown in Figs. 20c to 20f. As seen, the deformation modes in cross mixed and shear were somewhat similar. In mixed mode the screw was pushed sideways and pulled upwards by the top plate, causing the screw to rotate slightly and stressing the threads on the right side of the hole. In shear the screw was pushed sideways by the top plate, causing the screw to rotate significantly. However, in both simulations failure occurred later and the failure took place closer to the screw than in the experiments, which can be seen by comparing Figs. 20d and 20f with Figs. 6c and 6d, respectively. This is possibly explained by the Cockcroft-Latham failure model. As seen in Fig. 17, the model predicts a higher failure strain for pure shear and compressive stress states than under uniaxial tension (for which it was calibrated), and goes to infinity for pure compressive stress states. It has, however, been shown that for some ductile metals in the low stress triaxiality regime the failure strain does not increase monotonically with decreased hydrostatic stress (stress triaxiality) (Bao and Wierzbicki, 2004; Barsoum and Faleskog, 2007). In the cross mixed and cross shear test simulations the stress triaxiality in the area where failure took place in the experiments was low (≤ 0), suggesting that an over-estimation of the failure strain by the Cockcroft-Latham model was expected. Furthermore, as seen in Fig. 22 the stress state in the area where fracture took place in the cross shear experiment was purely compressive (negative main principal stress),

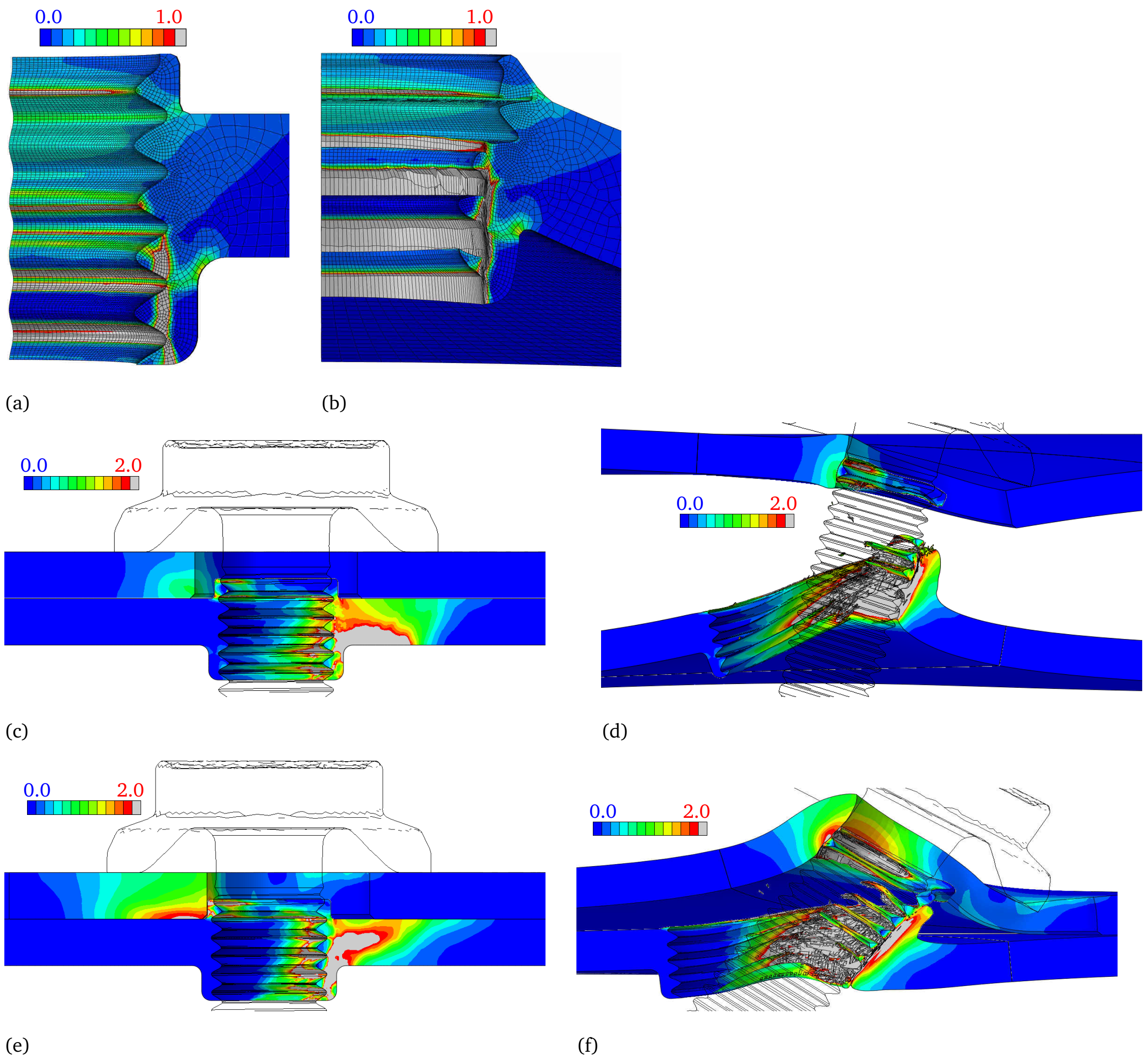

Fig. 20. Equivalent plastic strain field on undeformed and deformed configuration in (a and b) tension (right before failure), (c and d) mixed mode (last frame) and (e and f) shear (last frame).

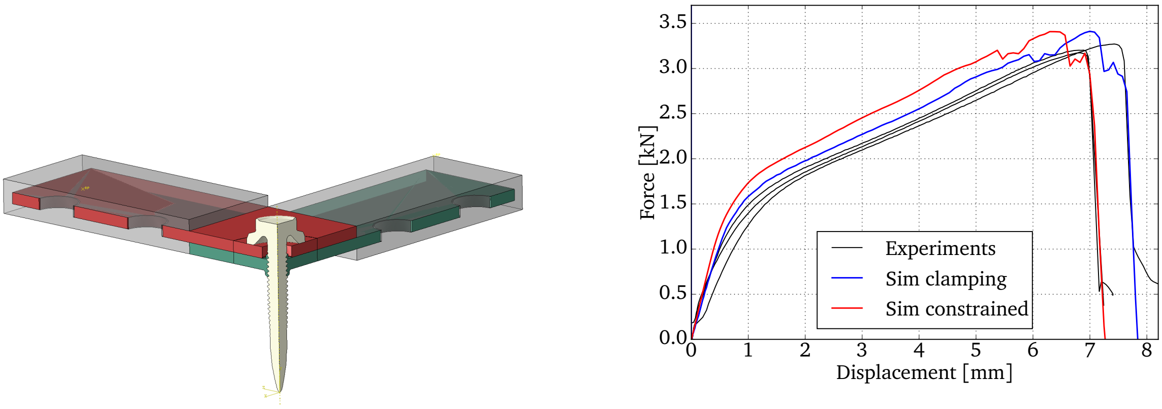

(a) (b)

Fig. 21. Finite element model to check the effect of the clamping. (a) Finite element model. (b) Force-displacement results compared to the original constrained simulation and experiments.

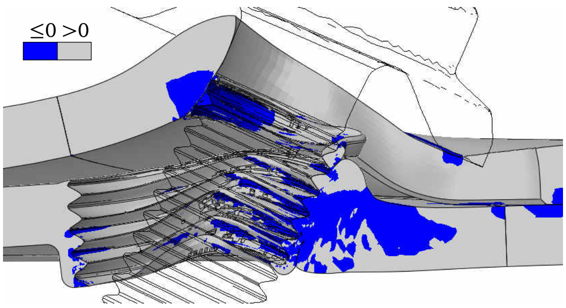

Fig. 22. Sign of main principal stress σ_1 at 8.9 mm displacement (time of maximum force) in the cross shear simulation. Blue colour indicates $\sigma_1 \leq 0$.

which implies that damage does not grow (Eq. (2)). Hence the failure model was not able to predict the failure mode of the experiments correctly, and fracture was forced to occur elsewhere (closer to the screw). However, the global results were nevertheless satisfactory. Thus such a model can still provide valuable information, and be used for e.g. calibration of macroscopic connection models.

5.2. Single lap-joint and peeling test simulations

Fig. 23a shows that the single lap-joint simulation agreed acceptably with the experiments. The maximum force was slightly over-estimated. In the experiments the maximum force occurred early (approximately 4 mm displacement) and the force decreased gradually until onset of failure, while in the simulation the force increased gradually from onset of plasticity to maximum force at approximately 8 mm displacement after which failure occurred abruptly. A good match was attained for the displacement at failure. The initial stiffness was reasonably predicted. This may possibly be attributed to the fact that the cross-head displacement was used as displacement

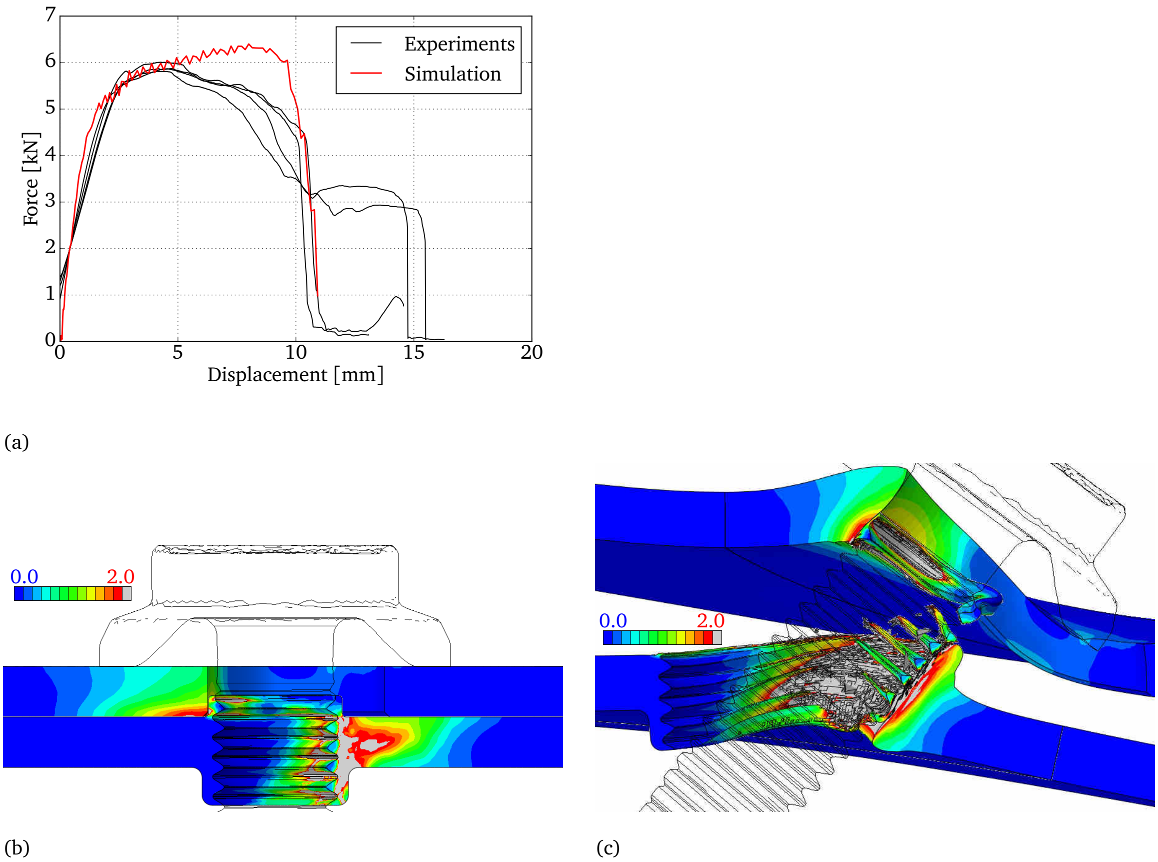

Fig. 23. Results from single lap-joint simulation. (a) Force-displacement curve. (b-c) Equivalent plastic strain field on undeformed and deformed configuration (last frame).

measure in the experimental tests, probably affected by compliance in the test set-up. Note that the experimental curves were shifted to coincide with the simulation at 2 kN force, as for the cross shear test simulations (see discussion above).

Figs. 23b and 23c depict the equivalent plastic strain field close to the screw at the end of the simulation on initial and deformed configurations, respectively. As seen when comparing with Figs. 20e and 20f the deformation was similar to the cross shear simulation. The less restrictive clamping in the single lap-joint test is clearly seen as the plates were further apart than in the cross shear simulation.

Favourable agreement was also obtained for the peeling simulation (Fig. 24a). The force level was generally satisfactory and the maximum force and displacement at failure were correctly predicted. The initial stiffness was slightly over-estimated, which, as for the single lap-joint tests, might be because the cross-head displacement was used as displacement measure in the experiments. It is also seen that the abrupt slope increase at 2 kN force caused by contact between the shaft of the screw and the bottom plate was well captured. Fig. 24b shows the deformed configuration at the time of maximum force, where the contact between the shaft of the screw and the

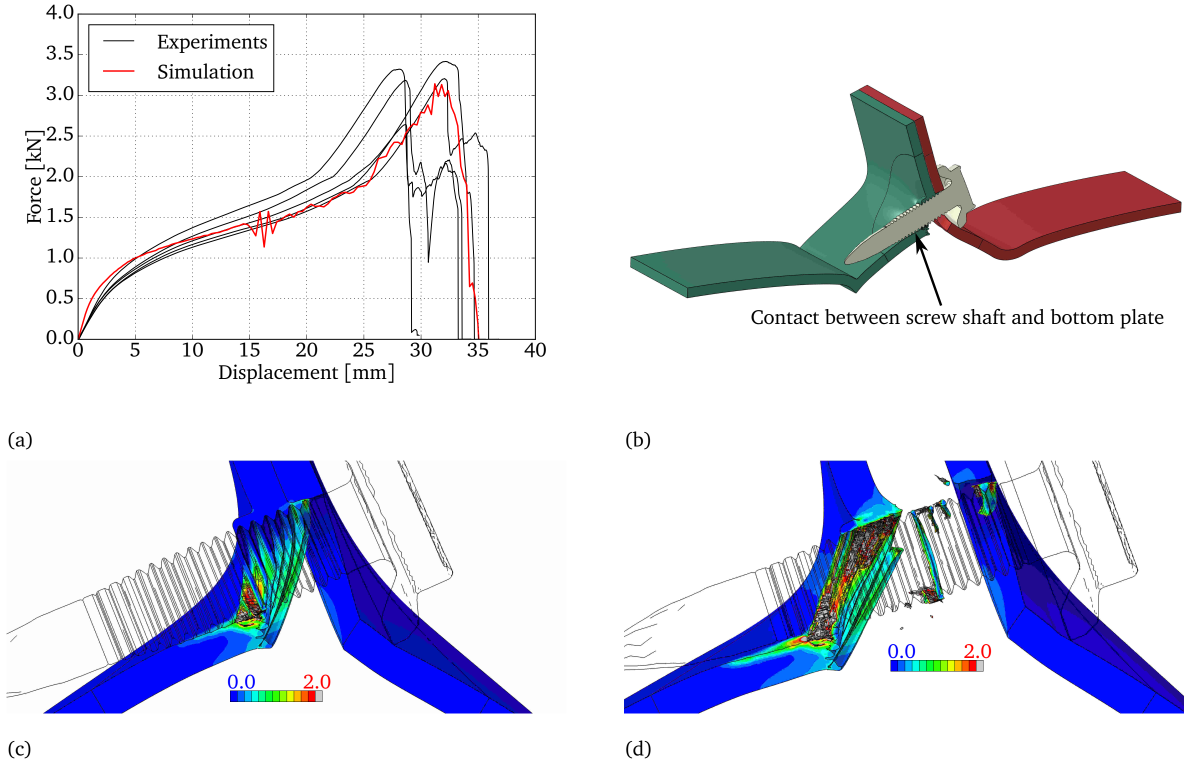

Fig. 24. Results from peeling simulation. (a) Force-displacement curve. (b) Deformed configuration at time of maximum force. (c) Equivalent plastic strain field at time of maximum force. (d) Equivalent plastic strain field after failure.

bottom plate is indicated. Figs. 24c and 24d show the equivalent plastic strain field at the time of maximum force and after failure, respectively. Failure occurred by stripping the still-engaged threads. The deformation mode and failure mechanism conformed to experimental observations.

5.3. Effect of friction coefficient

To evaluate the effect of the friction coefficient on the numerical results, the simulations were also carried out with friction coefficients of 0.0, 0.2 and 0.3, in addition to the original chosen value of 0.1. The coefficient was varied for three different contact interfaces independently, namely between the screw and the top plate, between the screw and the bottom plate, and between the two plates. It turned out that for tension loading the friction coefficient had a negligible effect, while it was most prominent for shear loadings. Only the curves from the cross shear simulations are therefore shown. The results are summarised in Fig. 25. As seen, there was an effect on the maximum force level, while limited effect was seen on the ductility of the connections. Moreover, the variation due to friction coefficient was in the same order as the variation on the experimental curves. This is natural, due to uncertainties in the process parameters, such as surface cleanliness, pre-stressing and so on, causing diversity in friction in the connections. Changes in the friction coefficient did not alter the deformation

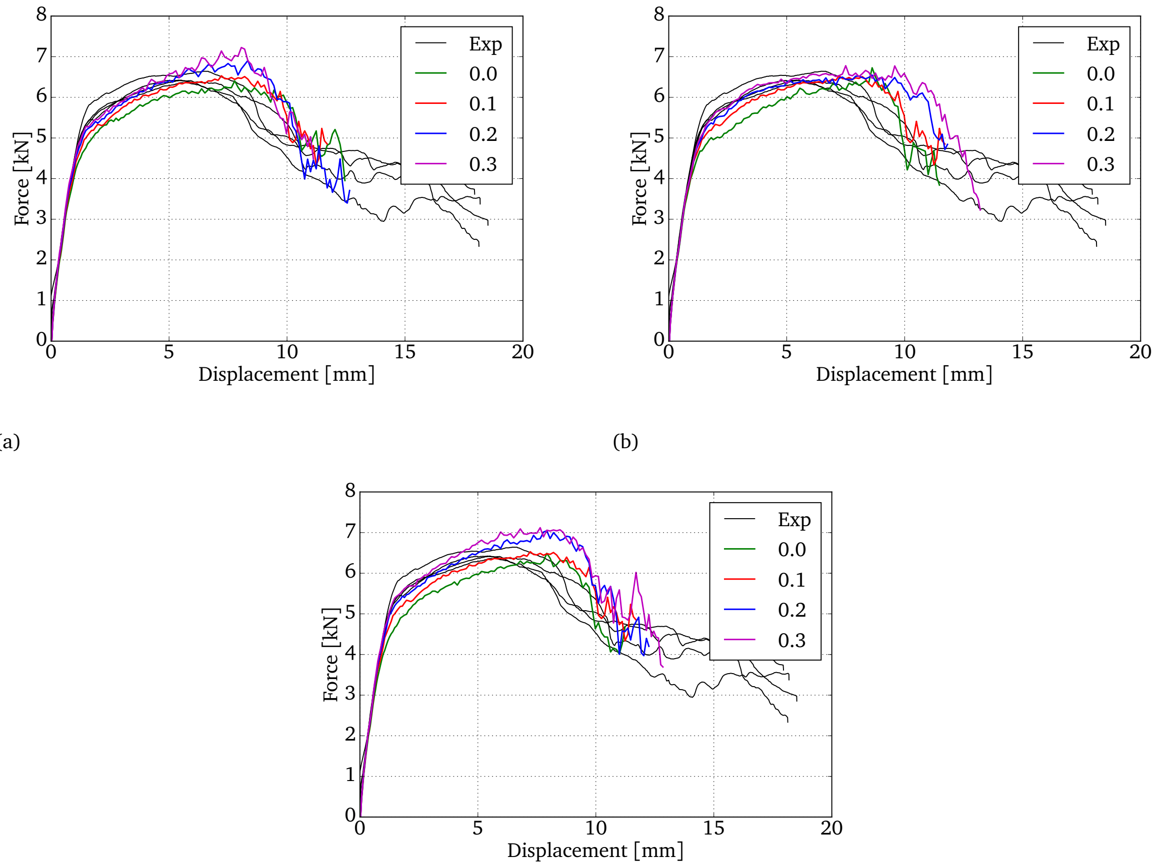

(a) (b) (c)

Fig. 25. The effect of friction coefficient on the global force-displacement curves in the cross shear simulation. The coefficient was varied at the contact interfaces between (a) the screw and top plate, (b) the screw and the bottom plate, and (c) between the plates.

modes significantly. Thus, changing the friction coefficients did not change the physics, the overall behaviour remained the same. Except for a slightly different maximum force, no conclusions would have changed if a friction coefficient of 0.3 had been chosen instead of 0.1.

6. Conclusions

In the present study the behaviour of flow-drill screw connections in quasi-static tests were simulated using finite element models with detailed solid element meshes. The experiments were described and presented in detail, including a new test set-up for cross tests. The numerical models were developed with a rate-independent isotropic hypoelastic-plastic material model. A simple approach for building up the geometry of the connection was presented. The following main conclusions may be drawn from the present investigation:

– A microstructural analysis indicated that the width of the plastically deformed zone due to the process is small. This was supported by Vickers hardness tests that showed no significant variation in the horizontal direction away from the screw.

– The finite element models gave satisfying results despite simplifications such as isotropic materials, simplified connection geometry, a simple failure criterion, and neglected process effects.

– Good matches between experimental and numerical global force-displacement curves were obtained for all tests.

– Overall deformation and failure modes agreed well with experiments. For shear-dominated loadings fracture tended to occur closer to the screw than in the experiments. This was attributed to the Cockcroft-Latham failure criterion's inability to account for damage at low stress triaxialities.

– Overall, the demonstrated modelling strategy was well-suited to investigate the behaviour of FDS connections under quasi-static loadings. This suggests that the approach may be used for virtual testing, for instance to calibrate macroscopic connection models for large-scale analyses.

Acknowledgements

Acknowledgements are made to Honda R&D Americas, Inc., and Centre for Advanced Structural Analysis (CASA), Department of Structural Engineering at Norwegian University of Science and Technology (NTNU) for financial support. Furthermore we would like to thank Matthias Reil, Tore Wisth, Trond Auestad and Dr. Hieu Nguyen Hoang for their contributions to parts of the work presented. This research has received funding from The Research Counsil of Norway, project number 237885.

References

Bao, Y., Wierzbicki, T., 2004. On fracture locus in the equivalent strain and stress triaxiality space. International Journal of Mechanical Sciences 46 (1), 81 – 98. https://doi.org/10.1016/j.ijmecsci.2004.02.006

Barsoum, I., Faleskog, J., 2007. Rupture mechanisms in combined tension and shear-experiments. International Journal of Solids and Structures 44 (6), 1768 – 1786, Physics and Mechanics of Advanced Materials. https://doi.org/10.1016/j.ijsolstr.2006.09.031

Björklund, O., Larsson, R., Nilsson, L., 2013. Failure of high strength steel sheets: Experiments and modelling. Journal of Materials Processing Technology 213 (7), 1103 – 1117. https://doi.org/10.1016/j.jmatprotec.2013.01.027

Bouchard, P., Laurent, T., Tollier, L., 2008. Numerical modeling of self-pierce riveting—from riveting process modeling down to structural analysis. Journal of Materials Processing Technology 202 (1), 290 – 300. https://doi.org/10.1016/j.jmatprotec.2007.08.077

Bridgman, P., 1944. The stress distribution at the neck of a tension specimen. Trans. ASM 32, 553–574.

Chen, J.-J., Shih, Y.-S., 1999. A study of the helical effect on the thread connection by three dimensional finite element analysis. Nuclear Engineering and Design 191 (2), 109 – 116. https://doi.org/10.1016/S0029-5493(99)00134-X

Chen, N., Luo, H., Wan, M., loup Chenot, J., 2014. Experimental and numerical studies on failure modes of riveted joints under tensile load. Journal of Materials Processing Technology 214 (10), 2049 – 2058. https://doi.org/10.1016/j.jmatprotec.2013.12.023

Cockcroft, M., Latham, D., 1968. Ductility and the workability of metals. J Inst Metals 96 (1), 33–39.

Fagerholt, E., 2012. Field measurements in mechanical testing using close-range photogrammetry and digital image analysis. Ph.D. thesis, Norges teknisk-naturvitenskapelige universitet (NTNU).

Grujicic, M., Snipes, J., Ramaswami, S., 2016. Process and product-performance modeling for mechanical fastening by flow drilling screws. International Journal of Structural Integrity 7 (3), 370–396. https://doi.org/10.1108/IJSI-03-2015-0011

Khadyko, M., Dumoulin, S., Hopperstad, O., 2016. Texture gradients and strain localisation in extruded aluminium profile. International Journal of Solids and Structures 97, 239 – 255. https://doi.org/10.1016/j.ijsolstr.2016.07.024

Kong, X., Yang, Q., Li, B., Rothwell, G., English, R., Ren, X., 2008. Numerical study of strengths of spot-welded joints of steel. Materials & Design 29 (8), 1554 – 1561. https://doi.org/10.1016/j.matdes.2007.12.001

Lademo, O.-G., Engler, O., Keller, S., Berstad, T., Pedersen, K., Hopperstad, O., 2009. Identification and validation of constitutive model and fracture criterion for AlMgSi alloy with application to sheet forming. Materials & Design 30 (8), 3005 – 3019. https://doi.org/10.1016/j.matdes.2008.12.020

Lademo, O.-G., Hopperstad, O., Langseth, M., 1999. An evaluation of yield criteria and flow rules for aluminium alloys. International Journal of Plasticity 15 (2), 191 – 208. https://doi.org/10.1016/S0749-6419(98)00064-3

Liu, C., Tan, K. H., Fung, T. C., 2015. Investigations of nonlinear dynamic performance of top-and-seat with web angle connections subjected to sudden column removal. Engineering Structures 99 (Supplement C), 449 – 461. https://doi.org/10.1016/j.engstruct.2015.05.010

Nielsen, K. L., Oct 2008. 3D modelling of plug failure in resistance spot welded shear-lab specimens (DP600-steel). International Journal of Fracture 153 (2), 125–139. https://doi.org/10.1007/s10704-008-9305-4

Nielsen, K. L., Tvergaard, V., 2010. Ductile shear failure or plug failure of spot welds modelled by modified Gurson model. Engineering Fracture Mechanics 77 (7), 1031 – 1047. https://doi.org/10.1016/j.engfracmech.2010.02.031

Porcaro, R., Hanssen, A., Langseth, M., Aalberg, A., 2006. The behaviour of a self-piercing riveted connection under quasi-static loading conditions. International Journal of Solids and Structures 43 (17), 5110 – 5131. https://doi.org/10.1016/j.ijsolstr.2005.10.006

Sabuwala, T., Linzell, D., Krauthammer, T., 2005. Finite element analysis of steel beam to column connections subjected to blast loads. International Journal of Impact Engineering 31 (7), 861 – 876. https://doi.org/10.1016/j.ijimpeng.2004.04.013

Skovron, J., Mears, L., Ulutan, D., Detwiler, D., Paolini, D., Baeumler, B., Claus, L., 09 2014. Characterization of Flow Drill Screwdriving Process Parameters on Joint Quality. SAE Int. J. Mater. Manf. 8, 35–44. https://doi.org/10.4271/2014-01-2241

Skovron, J. D., Prasad, R. R., Ulutan, D., Mears, L., Detwiler, D., Paolini, D., Baeumler, B., Claus, L., 2015. Effect of Thermal Assistance on the Joint Quality of Al6063-T5A During Flow Drill Screwdriving. Journal of Manufacturing Science and Engineering 137 (5), 051019. https://doi.org/10.1115/1.4031242

Sønstabø, J. K., Holmstrøm, P. H., 2013. Behaviour and modelling of self-piercing screw and self-piercing rivet connections: An experimental and numerical investigation. Master's thesis, Institutt for konstruksjonsteknikk, Norwegian University of Science and Technology (NTNU).

Sønstabø, J. K., Holmstrøm, P. H., Morin, D., Langseth, M., 2015. Macroscopic strength and failure properties of flow-drill screw connections. Journal of Materials Processing Technology 222, 1 – 12. https://doi.org/10.1016/j.jmatprotec.2015.02.031

Sønstabø, J. K., Morin, D., Langseth, M., 2016. Macroscopic modelling of flow-drill screw connections in thin-walled aluminium structures. Thin-Walled Structures 105, 185 – 206. https://doi.org/10.1016/j.tws.2016.04.013

Szlosarek, R., Karall, T., Enzinger, N., Hahne, C., Meyer, N., 2013. Mechanical testing of flow drill screw joints between fibre-reinforced plastics and metals. Materials Testing 55 (10), 737–742. https://doi.org/10.3139/120.110495